CHEMISTRY OF MATERIALS
Article

Chem. Mater. **2009,** *21,* 2967–2972 2967
DOI:10.1021/cm9007188

Response of the Crystal Structure and Electronic Properties to Calcium Substitution in NdFeAsO

A. Marcinkova,[†] E. Suard,[‡] A. N. Fitch,[§] S. Margadonna,[†] and J. W. G. Bos*,[†]

[†]*School of Chemistry and Centre for Science at Extreme Conditions, University of Edinburgh, Edinburgh EH9 3JJ, United Kingdom,* [‡]*Institut Laue Langevin, 38042 Grenoble, France, and* [§]*European Synchrotron Radiation Facility, 39043 Grenoble, France*

Received March 13, 2009. Revised Manuscript Received April 27, 2009

Synchrotron X-ray, neutron powder diffraction, magnetic susceptibility, and electrical resistance measurements were used to investigate the $Nd_{1-x}Ca_xFeAsO$ series. The solubility of calcium is limited to $0 \leq x \leq 0.05$. Within this interval, the iron arsenide layer contracts linearly in agreement with the hole doping of anti-bonding iron 3d-orbital states at the Fermi level. Depletion of the free charge carriers results in a transition to semiconducting behaviour. The iron spin-density wave (SDW) transition temperature is reduced from 140 K ($x = 0$) to 125 K ($x = 0.025$) to 130 K ($x = 0.05$). Long-range SDW ordering is only observed in neutron diffraction concomitant with that of the rare-earth sublattice ($T_{N,Nd} \approx 2$ K), revealing that the Nd ordering enhances the ordered Fe moment in spite of the large difference in ordering temperature. The transition to semiconducting behaviour results in a dramatic change in the magnitude and field dependence of the magnetoresistance (MR), which is much reduced ($R/R_0 = 1.6$ for $x = 0$, 1.03 for $x = 0.025$, and 1.06 for $x = 0.05$ at 5 K and in 9 Tesla) and becomes more linear for $x > 0$. Finally, MR is first observed at the onset of the structural $P4/nmm \rightarrow Cmma$ transition, and increases more rapidly below T_{SDW}, providing further evidence that the structural phase transition and SDW are linked.

Introduction

The discovery[1] of high-T_c superconductivity in $LaFeAsO_{1-x}F_x$ generated enormous scientific interest and led to the rapid exploration of other iron-based superconductors. Presently, four main groups are known: 1111 type RFeAsO and AeFeAsF,[1−5] 122 type $AeFe_2As_2$,[6−8] 111 type A_xFeAs,[9−11] and 11 type $FeSe_{1-d}$,[12,13] where R = La, Ce−Nd, Sm, Gd−Dy, Ae = Ba, Sr, Ca, Eu, and A = Li, Na. The 1111 and 122 materials share many features. Perhaps the most important one is that superconductivity emerges from a magnetically ordered metallic state by charge carrier doping.[14] In the RFeAsO materials, this may be achieved by electron and hole doping, whereas the $AeFe_2As_2$ materials become superconducting upon hole doping only. There is a wide variety of chemical ways for charge carrier doping into the conducting iron arsenide layers. This includes substitutions in the electronically inert layers, such as $(R_{1-x}Sr_x)$,[15] $(Ae_{1-x}K_x)$,[7] $(O_{1-x}F_x)$[1] and (O_{1-d}),[16] but also by direct doping on the Fe site by for example Co.[17] Hydrostatic pressure has also been used to suppress the magnetic ordering and induce superconductivity.[18] Band structure calculations show that the electronic states at the Fermi level are mostly made up out of Fe 3d orbital states with a small but non-zero contribution of the pnictide-atom.[19−21] The largest contribution is from the Fe $3d_{x^2-y^2}$ orbital, which points directly towards the nearest

*Corresponding author. E-mail: j.w.g.bos@ed.ac.uk.

(1) Kamihara, Y.; Watanabe, T.; Hirano, M.; Hosono, H. *J. Am. Chem. Soc.* **2008**, *130*, 3296.
(2) Chen, G. F.; Li, Z.; Wu, D.; Li, G.; Hu, W. Z.; Dong, J.; Zheng, P.; Luo, J. L.; Wang, N. L. *Phys. Rev. Lett.* **2008**, *100*, 247002.
(3) Chen, X. H.; Wu, T.; Wu, G.; Liu, R. H.; Chen, H.; Fang, D. F. *Nature* **2008**, *453*, 761.
(4) Matsuishi, S.; Inoue, Y.; Nomura, T.; Hirano, M.; Hosono, H. *J. Phys. Soc. Jpn.* **2008**, *77*, 113709.
(5) Matsuishi, S.; Inoue, Y.; Nomura, T.; Yanagi, H.; Hirano, M.; Hosono, H. *J. Am. Chem. Soc.* **2008**, *130*, 14428.
(6) Chen, G. F.; Li, Z.; Li, G.; Hu, W. Z.; Dong, J.; Zhou, J.; Zhang, X. D.; Zheng, P.; Wang, N. L.; Luo, J. L. *Chin. Phys. Lett.* **2008**, *25*, 3403.
(7) Sasmal, K.; Lv, B.; Lorenz, B.; Guloy, A. M.; Chen, F.; Xue, Y. Y.; Chu, C. W. *Phys. Rev. Lett.* **2008**, *101*, 107007.
(8) Rotter, M.; Tegel, M.; Johrendt, D. *Phys. Rev. Lett.* **2008**, *101*, 107006.
(9) Parker, D. R.; Pitcher, M. J.; Clarke, S. J. *Chem. Commun.* **2009**, 2189.
(10) Pitcher, M. J.; Parker, D. R.; Adamson, P.; Herkelrath, S. J. C.; Boothroyd, A. T.; Ibberson, R. M.; Brunelli, M.; Clarke, S. J. *Chem. Commun.* **2008**, 5918.
(11) Tapp, J. H.; Tang, Z. J.; Lv, B.; Sasmal, K.; Lorenz, B.; Chu, P. C. W.; Guloy, A. M. *Phys. Rev. B* **2008**, *78*, 060505.
(12) Hsu, F. C.; Luo, J. Y.; Yeh, K. W.; Chen, T. K.; Huang, T. W.; Wu, P. M.; Lee, Y. C.; Huang, Y. L.; Chu, Y. Y.; Yan, D. C.; Wu, M. K. *Proc. Natl. Acad. Sci., U.S.A.* **2008**, *105*, 14262.
(13) Margadonna, S.; Takabayashi, Y.; McDonald, M. T.; Kasperkiewicz, K.; Mizuguchi, Y.; Takano, Y.; Fitch, A. N.; Suard, E.; Prassides, K. *Chem. Commun.* **2008**, 5607.
(14) Zhao, J.; Huang, Q.; de la Cruz, C.; Li, S. L.; Lynn, J. W.; Chen, Y.; Green, M. A.; Chen, G. F.; Li, G.; Li, Z.; Luo, J. L.; Wang, N. L.; Dai, P. C. *Nat. Mater.* **2008**, *7*, 953.
(15) Kasperkiewicz, K.; Bos, J. W. G.; Fitch, A. N.; Prassides, K.; Margadonna, S. *Chem. Commun.* **2009**, 707.
(16) Kito, H.; Eisakt, H.; Iyo, A. *J. Phys. Soc. Jpn.* **2008**, *77*, 063707.
(17) Sefat, A. S.; Jin, R. Y.; McGuire, M. A.; Sales, B. C.; Singh, D. J.; Mandrus, D. *Phys. Rev. Lett.* **2008**, *101*, 117004.
(18) Alireza, P. L.; Ko, Y. T. C.; Gillett, J.; Petrone, C. M.; Cole, J. M.; Lonzarich, G. G.; Sebastian, S. E. *J. Phys.: Condens. Matter* **2009**, *21*, 012208.
(19) Singh, D. J.; Du, M. H. *Phys. Rev. Lett.* **2008**, *100*, 237003.
(20) Haule, K.; Shim, J. H.; Kotliar, G. *Phys. Rev. Lett.* **2008**, *100*, 226402.
(21) Kasinathan, D.; Ormeci, A.; Koch, K.; Burkhardt, U.; Schnelle, W.; Leithe-Jasper, A.; Rosner, H. *New J. Phys.* **2009**, *11*, 025023.

Published on Web 05/18/2009

neighbour Fe atoms and is highly dispersive in the $a-b$ plane but remains flat along the c-direction. The second largest contribution is from the xz and yz orbitals.[21] The origin of the magnetic ordering in the parent material remains under debate but is commonly attributed to a spin-density wave (SDW) instability at the Fermi surface.[22] Among the new high-T_c groups, the $RFeAsO_{1-x}F_x$ materials are of particular interest as they afford the highest critical temperatures and fields up to 55 K and ~100 T.[23−25]

Here we report on the crystal and magnetic structures, the magnetic susceptibilities, and electrical resistivities of the $Nd_{1-x}Ca_xFeAsO$ series. Substitution of Ca^{2+} on the Nd^{3+} site corresponds to nominal hole doping (oxidation of iron). The NdFeAsO parent is a poor metal that shows a separate (in temperature) SDW and tetragonal ($P4/nmm$) to orthorhombic ($Cmma$) transition. These transitions occur at 140 and 160 K, respectively. The magnetic ordering is confirmed by neutron powder diffraction, μSR, NMR, and Mossbauer with an ordered iron moment of ~0.25 μ_B.[26−30] The structural transition is second order and a broadening of synchrotron X-ray diffraction reflections is observed below 160 K, while full splitting is observed below 140 K.[30,31] There are two published neutron powder diffraction studies of the Fe SDW in NdFeAsO. One finds magnetic ordering below 2 K only, which coincides with the magnetic ordering of the Nd sublattice.[32] The refined moments are $m_x = m = 0.9(1)\,\mu_B$ for Fe and $m_x = 1.22(7)\,\mu_B$, $m_z = 0.96(9)\,\mu_B$, and $m = 1.55(4)\,\mu_B$ for Nd. In this case, the magnetic cell is identical to the crystallographic one and the Fe moments align in ferromagnetic stripes with the antiparallel alignment along the longer a-axis. The other demonstrates that the iron moments remain aligned in stripes up to $T_{SDW} = 141(6)$ K ($\gg T_{N,Nd} \approx 2$ K) but with a much reduced moment ($m = 0.25(7)\,\mu_B$) and a magnetic cell that is doubled along the c-axis.[29] The 3-fold increase in the ordered Fe moment below $T_{N,Nd}$ is unexpected, as the large difference in ordering temperatures suggests that the two sublattices do not interact much. Electron doping NdFeAsO via fluorine substitution or oxygen deficiency results in superconductivity with a maximum $T_c \approx 55$ K for in $NdFeAsO_{1-x}F_x$ and $NdFeAsO_{1-d}$.[16,33,34] In addition, these materials have upper critical fields on the order of 100 Tesla.[35] The pairing mechanism in these superconductors remains unclear but is likely related to the SDW, although measurements of the phonon density of states reveal small differences between parent and superconducting compositions in $NdFeAsO_{1-x}F_x$.[36] Hole doping via chemical substitution of Sr^{2+} on the Nd-site has been reported by some of us and affords a superconducting phase with $T_c = 15$ K for $x = 0.2$ in the series $Nd_{1-x}Sr_xFeAsO$.[15] The present study is part of our investigation into the chemical stability of the 1111-type materials and the effects that different dopants have on the crystal structure and physical properties of this important class of materials. To the best of our knowledge, this is the first detailed report on the effects of Ca doping in any of the 1111 type superconductors.

Experimental Section

Polycrystalline samples of $Nd_{1-x}Ca_xFeAsO$ were prepared using standard solid-state chemistry methods. Stoichiometric amounts of NdAs, FeAs, Fe, Fe_2O_3, and CaO were mixed intimately using mortar and pestle and pressed into dense pellets. These were heated for 24 hours at 1150 °C with one intermediate regrinding. All chemicals were obtained from Sigma Aldrich with at least 99.9% purity and all sample manipulations were done inside an Ar filled glovebox. The precursors FeAs and NdAs were prepared from stoichiometric mixtures of the elements heated in evacuated quartz tubes for 2 h at 500 °C, followed by 16 h at 900 °C for NdAs and 750 °C for FeAs. Laboratory powder X-ray diffraction using a Bruker D8 Advance diffractometer (Cu $K_{\alpha 1}$) revealed the presence of a CaO impurity phase for samples with $x > 0.15$. Traces of Nd_2O_3 or NdAs were observed for some attempts but never exceed 5 mass % from Rietveld fitting and are absent in the best samples. The initial exploration of these materials was done on a 0.5 g scale. For $x = 0$ and $x = 0.05$, 2 g samples were prepared for neutron powder diffraction measurements. Room-temperature synchrotron X-ray powder diffraction patterns were collected on the ID31 instrument at the European Synchrotron Radiation Facility, Grenoble. The prepared samples were measured during two experiments; the first with $\lambda = 0.39986$ Å was done on compositions $x = 0$, 0.05, and 0.10; the second with $\lambda = 0.40030$ Å was done on $x = 0.025$, 0.05, 0.075, and 0.15. The $x = 0.05$ sample was measured in both experiments for scaling purposes. Data sets were collected between $2 \le 2\theta \le 40°$ and binned with a stepsize of 0.002°. Rietveld fitting of these data sets showed that the solubility of calcium is limited to $x = 0.05$

(22) Mazin, II; Johannes, M. D.; Boeri, L.; Koepernik, K.; Singh, D. J. *Phys. Rev. B* **2008**, *78*, 085104.
(23) Bos, J. W. G.; Penny, G. B. S.; Rodgers, J. A.; Sokolov, D. A.; Huxley, A. D.; Attfield, J. P. *Chem. Commun.* **2008**, 3634.
(24) Ren, Z. A.; Lu, W.; Yang, J.; Yi, W.; Shen, X. L.; Li, Z. C.; Che, G. C.; Dong, X. L.; Sun, L. L.; Zhou, F.; Zhao, Z. X. *Chin. Phys. Lett.* **2008**, *25*, 2215.
(25) Ren, Z. A.; Yang, J.; Lu, W.; Yi, W.; Che, G. C.; Dong, X. L.; Sun, L. L.; Zhao, Z. X. *Mater. Res. Innovations* **2008**, *12*, 105.
(26) Aczel, A. A.; Baggio-Saitovitch, E.; Budko, S. L.; Canfield, P. C.; Carlo, J. P.; Chen, G. F.; Dai, P.; Goko, T.; Hu, W. Z.; Luke, G. M.; Luo, J. L.; Ni, N.; Sanchez-Candela, D. R.; Tafti, F. F.; Wang, N. L.; Williams, T. J.; Yu, W.; Uemura, Y. J. *Phys. Rev. B* **2008**, *78*, 214503.
(27) Carlo, J. P.; Uemura, Y. J.; Goko, T.; MacDougall, G. J.; Rodriguez, J. A.; Yu, W.; Luke, G. M.; Pengcheng Dai; Shannon, N.; Miyasaka, S.; Suzuki, S.; Tajima, S.; Chen, G. F.; Hu, W. Z.; Luo, J. L.; Wang, N. L. *Phys. Rev. Lett.* **2009**, *102*, 087001.
(28) McGuire, M. A.; Hermann, R. P.; Sefat, A. S.; Sales, B. C.; Jin, R.; Mandrus, D.; Grandjean, F.; Long, G. J. *New J. Phys.* **2009**, *11*, 025011.
(29) Chen, Y.; Lynn, J. W.; Li, J.; Li, G.; Chen, G. F.; Luo, J. L.; Wang, N. L.; Dai, P. C.; dela Cruz, C.; Mook, H. A. *Phys. Rev. B* **2008**, *78*, 064515.
(30) Jeglic, P.; Bos, J.-W. G.; Zorko, A.; Brunelli, M.; Koch, K.; Rosner, H.; Margadonna, S.; Arcon, D. *Phys. Rev. B* **2009**, *79*, 094515.
(31) Fratini, M.; Caivano, R.; Puri, A.; Ricci, A.; Ren, Z. A.; Dong, X. L.; Yang, J.; Lu, W.; Zhao, Z. X.; Barba, L.; Arrighetti, G.; Polentarutti, M.; Bianconi, A. *Supercond. Sci. Technol.* **2008**, *21*, 092002.
(32) Qiu, Y.; Bao, W.; Huang, Q.; Yildirim, T.; Simmons, J. M.; Green, M. A.; Lynn, J. W.; Gasparovic, Y. C.; Li, J.; Wu, T.; Wu, G.; Chen, X. H. *Phys. Rev. Lett.* **2008**, *101*, 257002.
(33) Chen, G. F.; Li, Z.; Wu, D.; Dong, J.; Li, G.; Hu, W. Z.; Zheng, P.; Luo, J. L.; Wang, N. L. *Chin. Phys. Lett.* **2008**, *25*, 2235–2238.
(34) Ren, Z. A.; Yang, J.; Lu, W.; Yi, W.; Shen, X. L.; Li, Z. C.; Che, G. C.; Dong, X. L.; Sun, L. L.; Zhou, F.; Zhao, Z. X. *Europhys. Lett.* **2008**, *82*, 57002.
(35) Jaroszynski, J.; Hunte, F.; Balicas, L.; Jo, Y. J.; Raicevic, I.; Gurevich, A.; Larbalestier, D. C.; Balakirev, F. F.; Fang, L.; Cheng, P.; Jia, Y.; Wen, H. H. *Phys. Rev. B* **2008**, *78*, 174523.
(36) Le Tacon, M.; Krisch, M.; Bosak, A.; Bos, J. W. G.; Margadonna, S. *Phys. Rev. B* **2008**, *78*, 140505.

(by refinement of the Nd/Ca occupancies). Variable-temperature high-resolution neutron powder diffraction data were collected on the high-resolution super-D2B powder diffractometer at the Insitut Laue Langevin in Grenoble, France. Data sets were recorded at 1.6 K and 175 K for $x = 0$ and $x = 0.05$. The instrument was used without additional collimation and with a large diameter beam to maximize the number of neutrons on the sample. The neutron wavelength used was $\lambda = 1.594$ Å. Data were recorded at $5 \leq 2\theta \leq 160°$ with a stepsize of 0.05°. High-flux neutron powder diffraction experiments were performed on the D20 instrument at the ILL.[37] The instrument was set up in the highest flux mode with $\lambda = 2.42$ Å. Data sets were collected over 4 h each at 1.6, 30, and 175 K in the $5 \leq 2\theta \leq 150°$ interval using a position sensitive detector. The GSAS suite of programs and the EXPGUI graphical user interface were used for Rietveld fitting of the synchrotron X-ray and neutron powder diffraction data.[38,39] The temperature dependences of the zero field cooled magnetic susceptibilities were measured in a field of 1 Tesla using a Quantum Design Magnetic Property Measurement System. The electrical resistance and magnetoresistance were measured in a standard four-point geometry using the resistance option of a Quantum Design Physical Property Measurement System. The dimensions of the bars were approximately $2 \times 1 \times 5$ mm^3.

Results

Crystal Structure. The synchrotron diffraction data were used to follow the x-dependence of the room temperature crystal structure. Rietveld fits for the $x = 0.025$ and $x = 0.05$ samples are shown in Figure S1 in the Supporting Information, whereas the fit for the $x = 0$ pattern is reported in ref 15. Increasing the Ca^{2+} content leads to an expansion of the *ab* plane, whereas the *c*-axis initially contracts and then increases slightly for $x = 0.05$ (Table 1). This results in an initial drop in cell volume followed by a modest increase (Table 1) and is consistent with the behavior observed in the $Nd_{1-x}Sr_xFeAsO$ series.[15] In contrast to these changes, the modification of the FeAs tetrahedral layers upon doping is systematic (Figure 1): First, the Fe−As distance decreases linearly upon increasing x, as is expected for hole doping (partial oxidation of Fe^{2+} to Fe^{3+}). Secondly, the Fe−As−Fe angle increases linearly, leading to a compression of the FeAs layer. The net effect of the shortened FeAs bond and increase in Fe−As−Fe angle is a linear decrease in the FeAs layer thickness (Fig. 1). The changes to the (Nd/Ca)−O and (Nd/Ca)−As bond lengths and angles are not linear but follow an increase−decrease (or decrease−increase) pattern, and are given in Table 1.

High-resolution neutron powder diffraction was used to follow the temperature dependence of the $x = 0$ and $x = 0.05$ samples. The data sets collected at 175 K could be indexed using the tetragonal $P4/nmm$ cell. Upon further cooling to 1.6 K, a tetragonal to orthorhombic structural transition occurs and both samples have low-temperature diffraction patterns consistent with the previously reported *Cmma* model for NdFeAsO.[31] A Rietveld fit for the $x = 0.05$ sample is given in Figure S2 in the Supporting Information. The refined lattice constants, atomic parameters, and selected bond length and angles are given

Table 1. Room Temperature Lattice Constants, Atomic Parameters, Selected Bond Lengths (Å) and Angles (deg), and Fit Statistics for the $Nd_{1-x}Ca_xFeAsO$ Series

		$x = 0$	$x = 0.025$	$x = 0.05$
a-axis (Å)		3.96594(1)	3.96773(1)	3.96805(1)
c-axis (Å)		8.59786(5)	8.58658(5)	8.58668(5)
V (Å^3)		135.233(1)	135.177(1)	135.201(1)
Nd	z	0.13888(6)	0.13935(6)	0.13894(7)
	occ	1.00	0.969(4)	0.950(5)
	U_{iso}	0.0068(2)	0.0057(2)	0.0045(2)
Ca	z		0.13935(6)	0.13894(7)
	frac		0.031(4)	0.050(5)
	U_{iso}		0.0057(2)	0.0045(2)
Fe	U_{iso}	0.0062(2)	0.0059(4)	0.0046(4)
As	z	0.6575(1)	0.6572(1)	0.6568(1)
	U_{iso}	0.0062(3)	0.0074(3)	0.0057(3)
O	U_{iso}	0.003(1)	0.016(2)	0.018(2)
Fe−As		2.4010(5)	2.3996(6)	2.3979(7)
As−Fe−As		111.36(4)	111.53(4)	111.66(5)
		108.54(2)	108.45(2)	108.39(2)
Nd−As		3.3061(5)	3.3045(6)	3.3087(7)
As−Nd−As		116.04(3)	116.18(3)	115.99(4)
Nd−O		2.3147(3)	2.3168(3)	2.3151(3)
O−Nd−O		117.89(2)	117.81(2)	117.96(2)
χ^2		2.0	2.1	2.1
wR_p (%)		15.2	18.1	18.1
R_p (%)		11.7	11.8	12.7
R_F^2 (%)		7.61	5.6	5.1

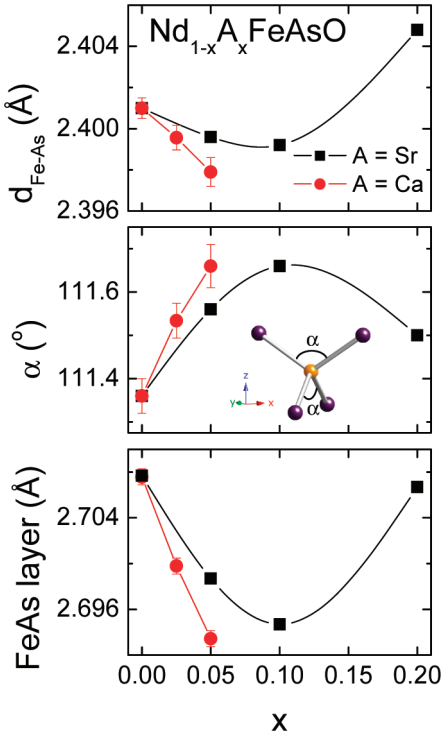

Figure 1. Doping dependence of the Fe−As bond distance, As−Fe−As tetrahedral angle, and FeAs layer thickness of the $Nd_{1-x}A_xFeAsO$ (A = Ca, Sr) series. The data for the Sr series are reproduced from our earlier work.[15]

(37) Hansen, T. C.; Henry, P. F.; Fischer, H. E.; Torregrossa, J.; Convert, P. *Meas. Sci. Technol.* **2008**, *19*, 034001.
(38) Larson, A. C.; Von Dreele, R. B. General Structure Analysis System (GSAS) ; Report LAUR 86-748; Los Alamos National Laboratory: Los Alamos, NM, 2000
(39) Toby, B. H. *J. Appl. Crystallogr.* **2001**, *34*, 210.

in Table 2. The structural transition leads to a rectangular distortion of the iron square planar sublattice (Table 2), which facilitates the long-range SDW ordering of the Fe moments.

Magnetic Susceptibilities. The inverse magnetic susceptibilities of the $Nd_{1-x}Ca_xFeAsO$ samples are shown in Figure 2 and are dominated by the (linear) paramagnetic contribution of the Nd^{3+} moments. This makes it difficult to asses the much smaller contribution of the iron moments to the magnetic susceptibility. A Curie−Weiss (CW) fit of the paramagnetic region was used to obtain an indication of the Nd^{3+} magnetism. The fitted Curie constants are given in the inset to Figure 2 as are the expected values for paramagnetic Nd^{3+} ($^4I_{9/2}$). The experimental values reveal a linear decrease in agreement with the partial replacement of magnetic Nd^{3+} with diamagnetic Ca^{2+}. However, the magnitude of the Curie constants is much larger than expected for $x = 0$ and $x = 0.025$, which may signal a significant contribution of the iron spins to the magnetic susceptibility, although the iron moments are not expected to show CW behavior. The experimental and calculated values are in good agreement for the most highly doped sample ($x = 0.05$). The Weiss temperatures are negative, indicative of antiferromagnetic interactions between Nd^{3+} spins, and are approximately −30 K for all x. We note that the CW model does not describe the magnetism in this system accurately and the results of the fits should therefore be treated with some caution.

Resistance. The temperature dependence of the resistance is shown in Figure 3. The $x = 0$ composition shows the typical drop below $T_{max} \approx 160$ K that is associated with the onset of the T→O structural transition, which is caused by the SDW transition that occurs around 140 K. The latter temperature corresponds to the maximum in dR/dT, which occurs at ∼140 K for our sample. The polycrystalline nature of our samples prevent us from making quantitative statements but it is evident that upon Ca^{2+} substitution, the temperature dependence of the resistance changes from metallic to semiconducting for $x = 0.025$ and remains semiconducting for $x = 0.05$. The drop in resistance observed for $x = 0$ is almost completely suppressed in the $x = 0.025$ materials but re-appears in the $x = 0.05$ composition. In fact, for $x = 0.025$, $dR/dT < 0$ over the entire measured temperature range, indicating semiconducting behavior, whereas the maximum slope occurs at ∼125 K. For $x = 0.05$, $T_{max} = 145$ K, whereas $(dR/dT)_{max} \approx 130$ K. These observations are consistent with a scenario where NdFeAsO is hole doped by substitution of Ca^{2+} leading to a depletion of free (n-type) charge carriers and thereby to semiconducting behaviour. This is qualitatively the same as the behaviour observed for the $Nd_{1-x}Sr_xFeAsO$ series with the distinction that Sr doping affords $x_{max} = 0.2$. At these higher doping levels, metallic conduction reappears, leading to superconductivity with $T_c = 15$ K.[15]

Magnetoresistance. The magnetoresistance of the $Nd_{1-x}Ca_xFeAsO$ samples was obtained from the measurement of R(H) curves between $-9\ T \le \mu_0 H \le 9\ T$. The as-measured curves were found to be slightly asymmetric for the $x = 0$ and $x = 0.05$ samples (inset to Figure 4), and in

Table 2. Lattice Constants, Atomic Parameters and Selected Bond Lengths (Å) and Angles (deg) for $Nd_{1-x}Ca_xFeAsO$ from Variable-Temperature D2B Neutron Powder Diffraction Data

		0		0.05	
		175	1.6	175	1.6
space group		*P4/nmm*	*Cmma*	*P4/nmm*	*Cmma*
a-axis (Å)		3.96133(4)	5.6154(1)	3.96351(5)	5.6157(1)
b-axis (Å)			5.5856(1)		5.5908(1)
c-axis (Å)		8.5772(2)	8.5591(2)	8.5662(2)	8.5479(2)
V (Å^3)		134.597(3)	268.461(7)	134.570(5)	268.372(6)
Nd/Ca	*z*	0.1389(2)	0.1390(2)	0.1388(2)	0.1389(2)
	U_{iso}	0.0036(7)	0.0004(6)	0.0023(6)	0.0005(6)
Fe	U_{iso}	0.0076(6)	0.0062(6)	0.0079(5)	0.0061(6)
As	*z*	0.6582(3)	0.6587(3)	0.6574(3)	0.6578(3)
	U_{iso}	0.0078(7)	0.0059(7)	0.0072(7)	0.0043(8)
O	U_{iso}	0.0061(8)	0.0049(8)	0.0050(7)	0.0049(6)
χ^2		2.4	2.4	2.9	2.8
wR_p (%)		5.2	5.2	5.9	5.7
R_p (%)		4.1	4.1	4.6	4.5
R_F^2 (%)		4.1	4.3	4.2	4.6
Fe−As		2.401(2)	2.401(2)	2.397(2)	2.397(2)
As−Fe−As		111.2(1)	111.1(1)	111.5(1)	111.5(1)
		108.64(5)	108.45(5)	108.45(5)	108.28(5)
			108.89(5)		108.65(5)
Nd−O		2.311(1)	2.310(1)	2.311(1)	2.310(1)
Nd−As		3.298(1)	3.299(1)	3.302(1)	3.302(1)
			3.286(1)		3.292(1)
Fe−Fe		2.80108(3)	2.80771(6)	2.80263(3)	2.80785(5)
			2.79280(6)		2.79538(5)

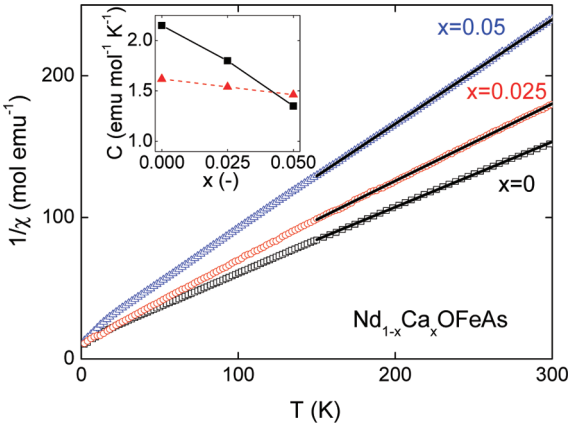

Figure 2. Inverse magnetic susceptibilities for the $Nd_{1-x}Ca_xFeAsO$ series. The inset shows a comparison between the experimental Curie constants (C) and the expected ones for Nd^{3+} ($^4I_{9/2}$).

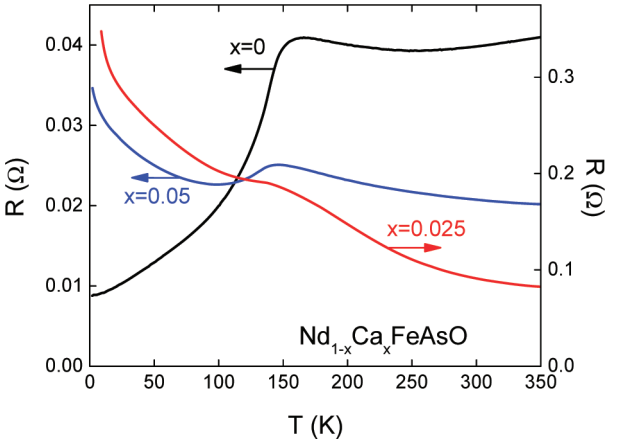

Figure 3. Temperature dependence of the electrical resistance for the $Nd_{1-x}Ca_xFeAsO$ series.

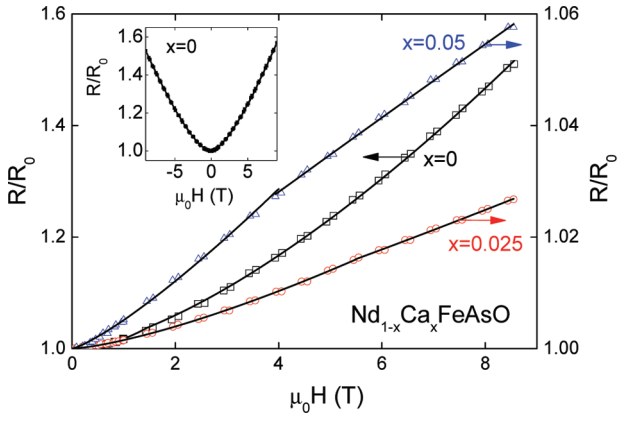

Figure 4. Magnetic field dependence of the magnetoresistance [$R/R_0 = R(H)/R(H=0)$] for the $Nd_{1-x}Ca_xFeAsO$ series at 5 K. The solid lines are power law fits to the data (see text). The inset shows the raw data collected for $x = 0$.

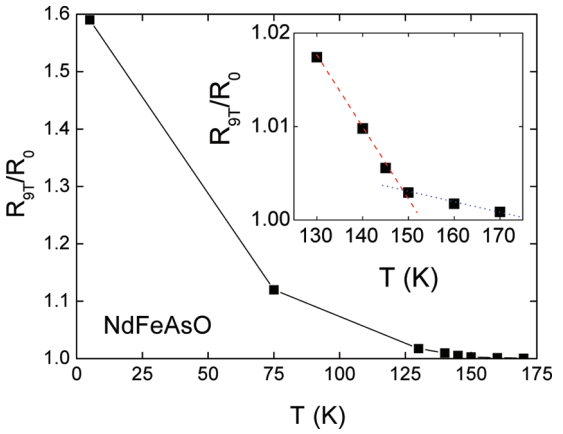

Figure 5. Temperature dependence of the magnetoresistance in 9 Tesla for NdFeAsO.

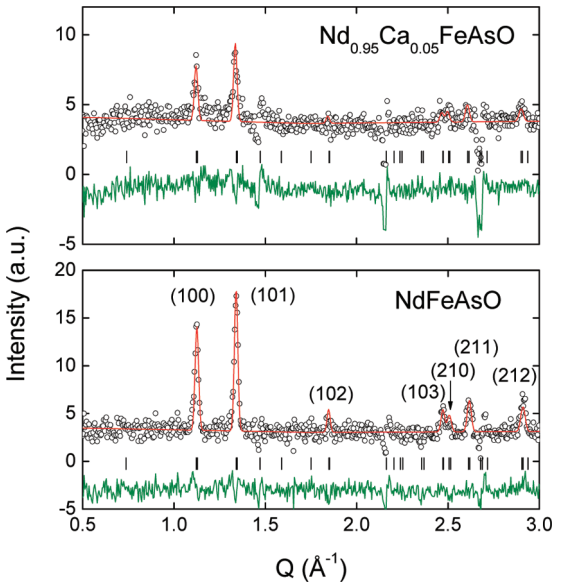

Figure 6. Rietveld fits to 2−30 K difference (magnetic contribution only) neutron diffraction patterns for $Nd_{1-x}Ca_xFeAsO$ ($x = 0$ and $x = 0.05$). The as-collected patterns are shown in Figure S3 of the Supporting Information.

the following, only the symmetric part of the MR response is given (Figure 4). The asymmetry arises from a Hall resistance due to the slight misalignment of the contact electrodes. The shape of the field dependence of the MR for the $x = 0$ sample is typical for a metallic conductor with an H^2 field dependence below $H = 1$ T. In larger applied fields, R/R_0 follows a power law with an exponent $n = 1.48$ (1). The solid lines in Figure 4 are fits. Upon Ca substitution, both the magnitude and shape of the MR change dramatically. The MR at 9 Tesla is 1.6 for $x = 0$, reduces to 1.03 for $x = 0.025$, and then increases to 1.06 for $x = 0.05$. At low fields, the MR is no longer quadratic and no longer typical of a metal. Furthermore a crossover in field dependence is visible at ~5.5 T for $x = 0.025$ and at ~4 T for $x = 0.05$ (Figure 4). For $x = 0.025$, power law fits yield $n = 1.38$ (1) for $0 \le \mu_0 H \le 5.5$ T and $n = 1.17(1)$ for $5.5 < \mu_0 H \le 8.5$ T. For $x = 0.05$, the values are n = 1.22(1) for $0 \le \mu_0 H \le 4$ T and $n = 0.96(1)$ for $4 < \mu_0 H \le 8.5$ T. These measurements reveal that the field dependence of R/R_0 becomes more linear for larger x and in larger applied magnetic fields. The temperature dependence of the 9 T MR for the $x = 0$ parent material is given in Figure 5. This reveals that the MR is largest at low temperatures and falls of with increasing temperature. In the vicinity of the SDW (~140 K) and structural transition (~160 K), two linear regions can be discerned. Small magnetoresistances are already observable upon the onset of the structural transition, whereas the MR increases more rapidly when the three-dimensional SDW ordering occurs. These observations show that the positive MR is related to the SDW ordering and provides further evidence that the structural transition and SDW are coupled. Our results are in excellent agreement with a recent single crystal study where $R/R_0 \approx 1.1$ at 75 K and 9 Tesla, revealing that the observed MR is intrinsic and not related to the polycrystalline nature of the samples.[40]

Magnetic Structure. Samples with $x = 0$ and $x = 0.05$ were studied using high-flux neutron powder diffraction. Identical counting times were used to collect data sets at 1.6, 30, and 175 K (see Figure S3 in the Supporting Information). These were carefully subtracted to separate the magnetic scattering from the structural contributions. The resulting 2−30 K difference patterns are shown in Figure 6. For $x = 0$, two strong and five weaker magnetic reflections were observed. These could all be indexed using the Cmma crystallographic cell. The intensities were fitted adequately using the combined Nd and Fe ordering model proposed by Qiu et al.[32] The refined moments are for Nd $m_x = 1.37(7)\,\mu_B$, $m_z = 1.31(8)\,\mu_B$, $m = 1.90(3)\,\mu_B$ and for Fe $m_x = 1.10(9)\,\mu_B$. Subtraction of the 175 K and 30 K patterns showed no magnetic reflections within the experimental accuracy (0.2−0.3 μ_B). For $x = 0.05$, the 2−30 K difference pattern (Figure 6) shows an identical magnetic diffraction pattern to that observed for $x = 0$. The reduction in intensities is consistent with a slightly lower ordering temperature of the Nd-sublattice resulting from the dilution of the magnetic Nd^{3+} lattice by non-magnetic Ca^{2+}. The refined moment are $m_x = 0.27(7)\,\mu_B$, $m_z = 0.42(5)\,\mu_B$, and $m = 0.50(2)\,\mu_B$ for Nd and $m_x = 0.27(5)\,\mu_B$ for Fe.

(40) Cheng, P.; Yang, H.; Jia, Y.; Fang, L.; Zhu, X. Y.; Mu, G.; Wen, H. H. *Phys. Rev. B* **2008**, *78*(13), 134508.

The 30−175 K difference pattern again showed no evidence for magnetic reflections within the experiment accuracy.

Discussion

The structures and properties of the $Nd_{1-x}Ca_xFeAsO$ series have been investigated. Synchrotron powder X-ray diffraction reveals that the $Nd_{1-x}Ca_xFeAsO$ series forms for $0 \leq x \leq 0.05$. This is substantially lower than $x_{max} = 0.20$ observed for the analogous Sr-series.[15] Both substitutions result in a formal $Fe^{(2+x)+}$ oxidation state but the sizes of the dopant cations are different. The ionic radius of Ca^{2+} is 1.12 Å, whereas that of Sr^{2+} is significantly larger at 1.26 Å. The radius for Nd^{3+} is tabulated as identical to that for Ca^{2+} (values for 8-fold coordination in oxides).[41] The structural response of the iron arsenide layer of the $Nd_{1-x}Sr_xFeAsO$ series has been included in Figure 1 to facilitate a comparison. It is evident that the magnitude of the changes in bond length, angle and layer thickness are comparable in the two series in spite of the different x_{max}. For the smaller Ca^{2+} cation a linear contraction in FeAs layer thickness is observed up to the maximum doping level $x = 0.05$, above which the structure is no longer stable. The larger Sr^{2+} cation reverses this trend, and for $x > 0.1$ the FeAs layer expands again. This expansion signals significant changes to the bonding that lead to the appearance of a superconducting state with $T_c = 15$ K for $x = 0.2$. At the moment, we cannot offer a good explanation for the difference in x_{max} between the two series.

The decrease in the FeAs layer thickness for $Nd_{1-x}Ca_xFeAsO$ is consistent with hole doping of the anti-bonding iron bands at the Fermi level. This results in a depletion of *n*-type charge carriers as evidenced by the transition from metallic to semiconducting behaviour (Fig. 3). The SDW transition remains intact and its transition temperature is reduced moderately. From $(dR/dT)_{max}$, T_{SDW} decreases from 140 K ($x = 0$) to 125 K ($x = 0.025$) and then increases to 130 K ($x = 0.05$). The presence of the SDW is confirmed by low-temperature neutron powder diffraction (Figure 6). Our results suggest a significant enhancement of the ordered Fe moment below $T_{N,Nd}$, which is surprising because of the weak coupling between the two sublattices as evidenced by the large difference between $T_{N,Nd}$ and T_{SDW}. In general, the small iron moments in the 1111 materials are not well understood, as electronic structure calculations consistently suggest that iron should have a moment of 1−2 μ_B.[22] Mazin and Johannes have suggested[42] that iron in fact has a large moment but that this appears strongly reduced because of fluctuations caused by antiphase boundaries and stacking faults along the *z*-direction. In this scenario, ordering of the Nd sublattice provides enhanced three-dimensional coherency and leads to observation of a larger Fe moment in neutron powder diffraction, consistent with our experimental results.

Magnetoresistance measurements (Fig. 5) reveal that the MR in the parent material first appears at the onset of the SDW transition (~160 K) and increases more rapidly when long range SDW ordering is fully established (below ~140 K). Ca substitution changes both the magnitude and field dependence of the MR. The MR is strongly reduced for the semiconducting samples suggesting that the concentration of free charge carriers is important. In conjunction, the field dependence of the MR changes from typical metallic to a near linear field dependence, with a transition evident near 5 Tesla for $x = 0.025$ and near 3.5 Tesla for $x = 0.05$. These measurements reveal that the MR is related to the SDW and the number of free charge carriers. The microscopic reason for the large positive MR is not well understood, which is not surprising given the debate of the nature of the SDW.[22,42] Generally, the magnitude of the MR is found to be larger in the 1111 RFeAsO parent materials than in the 122 $AeFe_2As_2$ group. The R/R_0 ratio in $BaFe_2As_2$ is ~1.1 at 5 K and 6.5 T compared to ~1.35 in NdFeAsO for the same conditions. This suggests that there might be a correlation with the ordered iron moment found from neutron powder diffraction, which is typically lower for the RFeAsO samples [0.25(7) μ_B for NdFeAsO compared to 0.87(3) μ_B for $BaFe_2As_2$],[43] or using the arguments above, that materials with stronger fluctuations (lower ordered Fe moment) have larger positive MR. It is worth pointing out that the MR shows an anomaly at the R-sublattice ordering temperature for R = Ce, Pr, and Nd, despite the absence of significant bonding between RO and FeAs layers.[28]

In conclusion: the substitution of Ca^{2+} in $Nd_{1-x}Ca_xFeAsO$ is possible for $0 \leq x \leq 0.05$ and results in a linear compression of the FeAs layer, which is consistent with a depletion of charge carriers from the anti-bonding electronic states at the Fermi level. This results in changes in the trends in resistance with temperature consistent with a transition from metallic to semiconducting behaviour as *x* increases, and is accompanied by a sharp reduction in the magnitude of the magnetoresistance, and a change to more linear field dependences with high-field transitions evident for the doped samples. The SDW transition temperatures are 140 K ($x = 0$), 125 K ($x = 0.025$) and 130 K ($x = 0.05$). Simultaneous Fe and Nd spin order is observed at 1.6 K, whereas no SDW ordering of the Fe spins could be detected at 30 K, revealing that ordering of the rare-earth sublattice strongly enhances the ordered iron moment.

Acknowledgment. J.W.G.B. acknowledges the Royal Society of Edinburgh for financial support and the EPSRC for provision of beam time at the ILL and ESRF. Andrew Huxley is acknowledged for scientific discussions.

Supporting Information Available: Rietveld fits to the room temperature synchrotron diffraction and 1.6 K neutron powder diffraction data. As-collected high-flux neutron powder diffraction patterns (PDF). This information is available free of charge via the Internet at http://pubs.acs.org.

(41) Shannon, R. D. *Acta Crystallogr., Sect. A* **1976**, *32*, 751.
(42) Mazin, II; Johannes, M. D. *Nat. Phys.* **2009**, *5*, 141.
(43) Huang, Q.; Qiu, Y.; Bao, W.; Green, M. A.; Lynn, J. W.; Gasparovic, Y. C.; Wu, T.; Wu, G.; Chen, X. H. *Phys. Rev. Lett.* **2008**, *101*, 257003.